

PAPER

Experimental identification of nonlinear coupling between (intermediate, small)-scale microturbulence and an MHD mode in the core of a superconducting tokamak

To cite this article: P.J. Sun *et al* 2018 *Nucl. Fusion* **58** 016003

View the [article online](#) for updates and enhancements.


Related content

- [Experimental study of the effect of 2/1 classical tearing mode on \(intermediate, small\)-scale microturbulence in the core of an EAST L mode plasma](#)
P J Sun, Y D Li, Y Ren *et al*.
- [Overview of experimental results on HL-2A](#)
X.R. Duan, X.T. Ding, J.Q. Dong *et al*.
- [Density fluctuation of geodesic acoustic mode on the HL-2A tokamak](#)
J. Cheng, L.W. Yan, K.J. Zhao *et al*.

Recent citations

- [Experimental study of the effect of 2/1 classical tearing mode on \(intermediate, small\)-scale microturbulence in the core of an EAST L mode plasma](#)
P J Sun *et al*
- [Influence of \$m / n = 2/1\$ magnetic islands on perpendicular flows and turbulence in HL-2A Ohmic plasmas](#)
M. Jiang *et al*

Experimental identification of nonlinear coupling between (intermediate, small)-scale microturbulence and an MHD mode in the core of a superconducting tokamak

P.J. Sun¹, Y.D. Li¹, Y. Ren², X.D. Zhang¹, G.J. Wu¹, L.Q. Xu¹, R. Chen¹, Q. Li³, H.L. Zhao¹, J.Z. Zhang¹, T.H. Shi¹, Y.M. Wang¹, B. Lyu¹ , L.Q. Hu¹, J. Li¹ and The EAST Team¹

¹ Institute of Plasma Physics, Chinese Academy of Sciences, Hefei 230031, People's Republic of China

² Princeton Plasma Physics Laboratory, Princeton, New Jersey 08543, United States of America

³ Guangdong University of Technology, Guangzhou 510006, People's Republic of China

E-mail: sunpj@ipp.ac.cn

Received 3 March 2017, revised 30 August 2017

Accepted for publication 6 September 2017

Published 1 November 2017



CrossMark

Abstract

In this paper, we present clear experimental evidence of core region nonlinear coupling between (intermediate, small)-scale microturbulence and an magnetohydrodynamics (MHD) mode during the current ramp-down phase in a set of L-mode plasma discharges in the experimental advanced superconducting tokamak (EAST, Wan *et al* (2006 *Plasma Sci. Technol.* **8** 253)). Density fluctuations of broadband microturbulence ($k_{\perp} \rho_i \sim 2-5.2$) and the MHD mode (toroidal mode number $m = -1$, poloidal mode number $n = 1$) are measured simultaneously, using a four-channel tangential CO₂ laser collective scattering diagnostic in core plasmas. The nonlinear coupling between the broadband microturbulence and the MHD mode is directly demonstrated by showing a statistically significant bicoherence and modulation of turbulent density fluctuation amplitude by the MHD mode.

Keywords: nonlinear coupling, multi-scale, density fluctuation, microturbulence

(Some figures may appear in colour only in the online journal)

1. Introduction

Microturbulence is considered as the major mechanism underlying anomalous transport in tokamak plasmas. The free energy to drive microturbulence can come from temperature gradients (i.e. ion temperature gradient (ITG) and electron temperature gradient (ETG)) and density gradients which universally exist in tokamak plasmas. Some well-known micro-instabilities are ITG mode [1], trapped electron mode (TEM) [2], ETG mode [3, 4] and micro-tearing mode [5-7]. In addition to being driven by equilibrium gradients, microturbulence can also interact nonlinearly with macro-instabilities, e.g. kink/tearing modes and edge localized mode [8], either through temperature and/or density profile modulations from macro-instabilities or through nonlinear cascade process [9].

Nonlinear interaction between microturbulence and macro-instabilities introduces new phenomena, e.g. self-organization [10] and formation of regular structure [11], and as a result, anomalous plasma transport can be affected. Understanding this nonlinear interaction is not only important for predicting and improving the confinement performance of future fusion devices, e.g. FNSF [12] and ITER [13], but also important for their safe operation, since understanding plasma transport with the presence of macro-instabilities is important, particularly during the current ramp-up and ramp-down phases, in order to avoid plasma disruption. In the literature, there are extensive reports on studies of individual effects of microturbulence and macro-instabilities on plasma confinement [14-22]. However, much less effort has been spent on their interactions. In general, the scale of microturbulence can

be divided into large-scale ($k_{\perp}\rho_i \leq 1$), intermediate-scale ($k_{\perp}\rho_i \sim 1-3$) and small-scale ($k_{\perp}\rho_i \geq 3$) [23], where k_{\perp} and ρ_i are perpendicular wavenumber and ion gyroradius respectively. Studies of nonlinear interaction between MHD modes and large-scale (low- k) microturbulence in theories and simulations are reported in [24–26], wherein it was found that macroscopic MHD modes and large-scale microturbulence can interact with each other both directly and indirectly, through meso-scale structures such as zonal flows. An experimental observation of nonlinear coupling between a long-wavelength mode (poloidal mode number $m = 12$) and large-scale ($\bar{k}_{\theta} = 3 \text{ cm}^{-1}$, $k_{\perp}\rho_i \leq 0.15$) microturbulence in TEXT tokamak edge plasmas is reported in [27]. The physical relationship between naturally occurring $m = 2$ tearing mode and non-localized measurement of large-scale ($k_{\theta} = 7, 9, 12 \text{ cm}^{-1}$, $0.4 \leq k_{\theta}\rho_s \leq 0.7$, $k_{\perp}\rho_i \approx k_{\theta}\rho_s$, where k_{θ} , ρ_s are poloidal wavenumber and ion gyroradius at electron temperature respectively) microturbulence in TEXT have been given in [28]. One recently published paper [29] reports the observation of localized modulation of large-scale ($k_{\theta} < 1 \text{ cm}^{-1}$, $k_{\perp}\rho_i < 0.4$) turbulent density fluctuations \tilde{n}_e by neoclassical tearing mode (NTM) in the core of DIII-D plasmas, following which an extended paper has been published in [30]. A newly published paper [31] in experiment and simulation gives the high correlation between microturbulent radial correlation length and magnetic islands. However, a direct identification of the nonlinear interaction between (intermediate, small)-scale microturbulence ($k_{\perp}\rho_i \sim 2-5.2$) and macro-instabilities in the core of high temperature tokamak plasmas has not been reported. We emphasize that such a study requires simultaneous measurement of both the (intermediate, small)-scale microturbulence and macro-instability in a spatial region. In this paper, we report a clear experimental identification of core region nonlinear coupling between (intermediate, small)-scale microturbulence and an MHD mode during the current ramp-down phase in a set of L-mode plasma discharges in EAST. A four-channel tangential CO₂ laser collective scattering diagnostic is used to make simultaneous measurements of density fluctuations of (intermediate, small)-scale microturbulence ($k_{\perp} = 10, 18$ and 26 cm^{-1} , $k_{\perp}\rho_i \sim 2-5.2$) and the MHD mode ($n = 1$ and $m = -1$ with mode frequency $f \approx 2-4 \text{ kHz}$). Using bispectral analysis [32], envelope [33] and cross-correlation methods, we identified the nonlinear coupling between (intermediate, small)-scale microturbulence and the MHD mode by demonstrating a statistically significant bicoherence, and modulations of turbulent density fluctuation amplitude in correlation with the MHD mode.

This paper is organized as follows. Experimental apparatus is detailed in section 2. In section 3, we present experimental observations, qualitative identification of the nonlinear coupling and discussion, which includes overview of the discharges and experimental observations (see section 3.1); qualitative identification of the nonlinear coupling and discussion (see section 3.2). A summary is given in section 4.

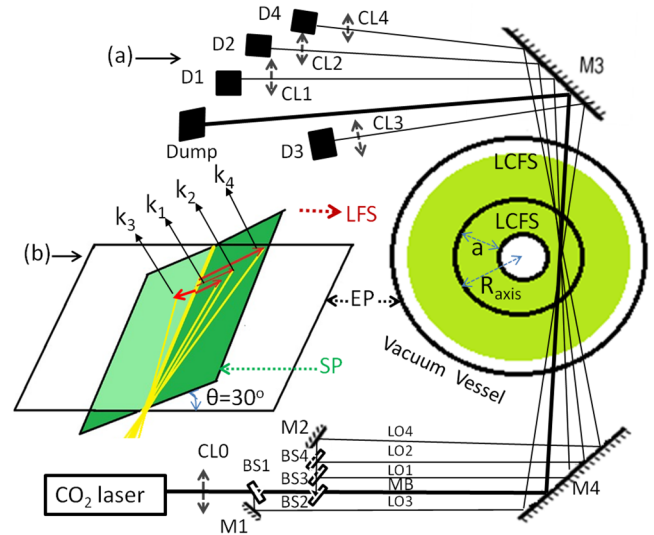


Figure 1. (a) Schematic of the CO₂ laser collective scattering system on EAST, where ‘BS’ denotes beam splitter, ‘M’ denotes mirror, ‘CL’ denotes converging lens, ‘LO’ denotes local oscillator and ‘D’ denotes detector. (b) The schematic of scattering configuration. The scattering plane (SP), where all the scattering wavenumber vectors lay in, is tilted with respect to the midplane (EP) with an angle of 30 degrees. Note that scattering wavenumbers \mathbf{k}_1 and \mathbf{k}_3 have the same wavenumber but lay on the different side of the main beam (MB).

2. Experimental apparatus

Plasma electron density fluctuations can be measured by the electromagnetic wave collective scattering diagnostics. The scattered power P_s from this diagnostics is proportional to the intensity of turbulent density fluctuation, according to the formula $P_s = \frac{1}{4}P_i r_e^2 \lambda_i^2 \tilde{n}_e^2 L_v^2$, when the incident electromagnetic wave (\vec{k}_i, ω_i), scattered electromagnetic wave (\vec{k}_s, ω_s) and density fluctuation (\vec{k}, ω) satisfy energy and momentum conservation, i.e. $\omega = \omega_s - \omega_i$ and $\vec{k} = \vec{k}_s - \vec{k}_i$, where P_i is the incident power, r_e is the classical radius of electrons, λ_i is the wavelength of incident electromagnetic wave, \tilde{n}_e is electron density fluctuation, L_v is the length of scattering volume. Moreover, since in the context at hand $\omega_s \approx \omega_i$ and $k_s \approx k_i$, the scattering angle θ_s must satisfy the Bragg condition, i.e. $k = 2k_i \sin(\theta_s/2)$. The measurement of density fluctuations in EAST was carried out with a four-channel tangential CO₂ laser collective scattering system, which is similar to the multi- k (poloidal) CO₂ laser collective scattering system in the HT-7 tokamak [34, 35]. Figure 1(a) shows the schematic of the scattering system. The main beam (MB) with input power $P_i \approx 10 \text{ W}$ is used as the scattering beam (single mode TEM₀₀, Gaussian beam, focused to the detection region by a converging lens CL0), and ‘Local Oscillator’ beams (LO1, LO2, LO3 and LO4) together with scattered lights are focused onto HgCdTe detectors through converging lenses (CL1, CL2, CL3 and CL4). This diagnostic provides homodyne measurement of density fluctuations up to 1 MHz

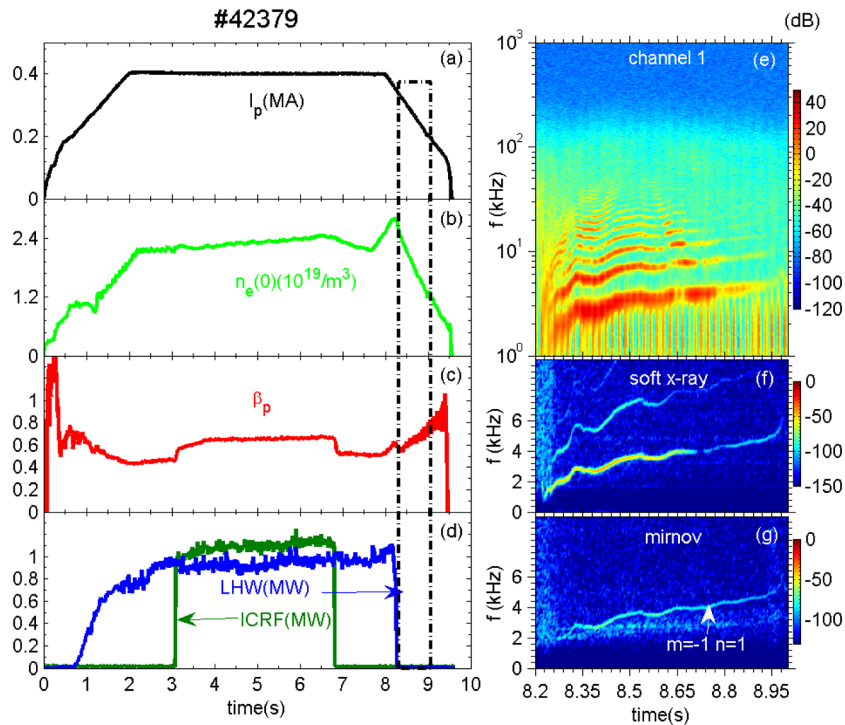


Figure 2. An overview of shot 42379: (a) plasma current; (b) line-averaged electron density; (c) poloidal beta; (d) lower hybrid wave (LHW) and ion cyclotron range of frequency (ICRF) heating power. Spectrograms of signals from (e) Channel 1 of the scattering system, (f) a channel of soft x-ray and (g) a low-frequency Mirnov coil for the time range of interest ($t = 8.2-9$ s); note that panel (e) has a logarithmic scale in y-axis and a linear scale in x-axis. The dash-dotted rectangles in panels (a)–(d) denote the time range of interest, $t = 8.2-9$ s.

and with perpendicular wave-number, k_{\perp} , ranging from 10 cm^{-1} to 30 cm^{-1} . In the experiment described below, MB lays nearly in the midplane (EP) and the scattering plane (SP) is tilted relative to the midplane with an angle of 30° (see figure 1(b)). Although the maximum scattering angle θ_s is less than 0.3° , due to its tangential scattering scheme [36, 37], the scattering system can make localized measurement of anisotropic density fluctuations with $k_{\parallel} \approx 0$ (k_{\parallel} being the parallel wavenumber along the local equilibrium magnetic field) with a radial resolution of $\pm 1 \text{ cm}$ determined by the waist radius of the laser beam ($w \approx 1 \text{ cm}$). The scattering system measures mostly radial wavenumber, k_r , much larger than poloidal wavenumber, k_{θ} , with a wavenumber resolution of about 2 cm^{-1} . The scattering location and scattering volume are calculated with a ray tracing code using an EFIT equilibrium reconstruction [38]. For the experiment shown in the rest of this paper, the scattering location is at $R_{\text{sca}} = 165.8 \text{ cm}$ ($\rho \approx 0.5$) on the high field side (HFS). Another advantage of this diagnostic is that coherent MHD modes, e.g. tearing mode, internal kink mode and energetic particle mode, can also be measured through the LO beam laser far-forward scattering mechanism [39, 40]. Since the frequency of CO_2 laser, i.e. $f \approx 2.8 \times 10^{13} \text{ Hz}$, is much larger than the electron plasma frequency $f \sim 10^{10} \text{ Hz}$ in EAST, there is no cut-off layer, and both the refraction and reflection effects can be negligible [37] for our EAST tangential CO_2 laser collective scattering scheme. Therefore, the wavenumber k of density fluctuation only depends on the scattering angle θ_s .

3. Experimental observations, qualitative identification of the nonlinear coupling and discussion

3.1. Overview of the discharges and experimental observations

Figure 2 shows an overview of a typical discharge for which we have done extensive analysis. The set of L-mode deuterium plasmas in which the observation was made has lower single null (LSN) configuration, plasma current of 400 kA (see figure 2(a)) and toroidal magnetic field of 2 T. The time range of interest is $t = 8.2-9$ s (see the dash-dotted rectangles in figures 2(a)–(d)) where the plasma current ramps down at a rate about 200 kA s^{-1} and the line-averaged electron density (figure 2(b)) decreases almost linearly. The poloidal beta, on the other hand, has an initial drop from 0.63 to 0.55 and then increases to 0.75 (figure 2(c)). Auxiliary heating from LHW and ICRF are both turned off before the time range of interest (figure 2(d)). Figures 2(e)–(g) show spectrograms for the signals from Channel 1 of the scattering system, a channel of soft x-ray measurements, and a low-frequency Mirnov coil, respectively. A low-frequency MHD mode can be identified from the multiple harmonics seen in figure 2(e) (We note that all channels of the scattering system measured this MHD mode), which presents the non-sinusoidal nature. This MHD mode also can be seen in the soft x-ray measurement in figure 2(f) and the Mirnov measurement in figure 2(g) as well. We note that only one harmonic is seen in the soft x-ray

measurement and no harmonic is seen in the Mirnov measurement. The possible reason for no harmonics in Mirnov measurement is that the magnetic fluctuation amplitude of higher frequencies (corresponding to higher mode numbers) from the harmonics decrease faster versus radial coordinate r as $B(r_p) \sim B(r) * (r/r_p)^{m+1}$, where r is the mode location and r_p is the Mirnov coil location. Fundamental frequency of this MHD mode ($m = -1$ and $n = 1$ identified using mirnov coil arrays and propagating in the electron diamagnetic drift direction in the laboratory frame of reference) increases from 1 kHz to 4.8 kHz in the time range of interest (the 50 Hz bursting spikes seen at the bottom of figure 2(e) are most likely due to AC interference). The multiple harmonics from the MHD mode, measured by LO beam laser far-forward scattering mode, can be clearly seen for $f < 50$ kHz in figure 2(e). Broadband microturbulence from main beam laser forward scattering mode can be identified at higher frequencies, i.e. $f > 50$ kHz, in figure 2(e) (the turbulent nature of higher frequency components is supported by a power-law falloff in the frequency spectrum at even higher frequencies, i.e. $f > 80$ kHz (not shown)) and its power is much weaker than the MHD mode, as expected (small wavenumber features which have large power). Power reserval versus frequency f at the frequency $f \approx 50$ kHz (not shown) more clearly supports that division, i.e. $f < 50$ kHz scattering signals from the MHD mode and $f > 50$ kHz ones from broadband turbulence.

3.2. Qualitative identification of the nonlinear coupling, and discussion

In the rest of this paper, we will identify the nonlinear interaction between (intermediate, small)-scale microturbulence and the MHD mode using bispectral analysis [32], envelope [33] and cross-correlation methods.

Firstly, we will use the spectral analysis method to identify the three-wave nonlinear coupling between the MHD mode and different scales of microturbulence from the corresponding detection channel of scattering signals. The bispectral analysis can quantify the intensity of three-wave coupling which satisfies the momentum and energy conservation conditions: $\vec{k}_3 = \vec{k}_1 \pm \vec{k}_2$ and $f_3 = f_1 \pm f_2$, where $\vec{k}_{1,2,3}$ are wavenumbers and $f_{1,2,3}$ are frequencies. This method has been successfully applied to fluctuation signals in tokamak experiments for identifying the nonlinear coupling among different modes [27, 33, 41, 42], and it will be described briefly below. The squared auto-bicoherence used in the bispectral analysis is defined as $b_{s,s,s}^2(f_1, f_2) = \frac{|B_{s,s,s}(f_1, f_2)|^2}{\langle |s(f_1)s(f_2)|^2 \rangle \langle |s(f_3)|^2 \rangle}$. The auto-bispectrum, i.e. $B_{s,s,s}(f_1, f_2) = \langle s(f_1)s(f_2)s^*(f_3) \rangle$, is a third order cumulant spectrum, where $s(f)$ is the Fourier component of the observed time-series $s(t)$, and the symbol $\langle \rangle$ denotes the ensemble average. We note that the squared auto-bicoherence is always between 0 and 1. The summed bicoherence, i.e. $\Sigma b_{s,s,s}^2(f_3) = \Sigma_{f_3=f_1+f_2} b_{s,s,s}^2(f_1, f_2)/N$, measures the amount of coupling at the frequency f_3 , i.e. we sum over all frequencies satisfying the resonance condition $f_3 = f_1 + f_2$ and normalized by the ensemble number N of

Fourier component for each f_3 in the summations. The bispectral analysis is carried out for the time period of $t = 8.63-8.73$ s with ensemble numbers $N = 200$ and frequency resolution $\Delta f = 1$ kHz, i.e. time window $\Delta t = 1$ ms, which means that the spectral analysis is time averaged over several fundamental MHD periods (the fundamental MHD frequency is $f \approx 4$ kHz here). Note that the red dotted lines denote the noise level $1/N = 0.05$ in figures 3(b)-(c) and (e)-(f), and the power of both the MHD mode and microturbulence are at quasi-steady state in that time period. The squared auto-bicoherence $b_{\tilde{n}_e, \tilde{n}_e, \tilde{n}_e}^2(f_1, f_2)$ of channel 1 ($k_1 = 10$ cm⁻¹) and channel 4 ($k_4 = 26$ cm⁻¹) as a function of frequencies f_1 and f_2 is shown in figures 3(a) and (d) respectively. We note that (a) and (d) share the same colorbar in figure 3. When f_2 is around -4 kHz, many bright parts (significant squared auto-bicoherence value) can be observed at frequencies such as $f_1 \approx 4$ kHz, 8 kHz, 16 kHz, 50–130 kHz ($k_1 = 10$ cm⁻¹, see figure 3(a)) and $f_1 \approx 4$ kHz, 8 kHz, 16 kHz, 100–300 kHz ($k_4 = 26$ cm⁻¹—see figure 3(d)). These indicate a significant level of nonlinear interaction concentrates at these frequencies. The summed squared auto-bicoherence $\Sigma b_{\tilde{n}_e, \tilde{n}_e, \tilde{n}_e}^2(f_3)$ are plotted in figures 3(b) and 3(e) for channel 1 and channel 4 respectively. Obvious $\Sigma b_{\tilde{n}_e, \tilde{n}_e, \tilde{n}_e}^2(f_3)$ peaks occur at the fundamental frequency $f_3 \approx 4$ kHz, as well as harmonic frequencies of the MHD mode in both figures 3(b) (channel 1) and 3(e) (channel 4). Moreover, the $\Sigma b_{\tilde{n}_e, \tilde{n}_e, \tilde{n}_e}^2(f_3)$ is slightly more than the noise level in the broad-band $f_3 \sim 50 - 130$ kHz for $k_1 = 10$ cm⁻¹ microturbulence (see figure 3(b)) as well as $f_3 \sim 100 - 300$ kHz for $k_4 = 26$ cm⁻¹ microturbulence (see figure 3(e)). These suggest that the fundamental MHD mode couples with both its harmonics and broad-band microturbulence for scales at $k_{\perp} = 10, 26$ cm⁻¹. In order to further verify and better observe the nonlinear coupling between the fundamental MHD mode and broad-band microturbulence, we fix the $f_3 = f_1 + f_2 = 4$ kHz, i.e. $f_2 = 4$ kHz $- f_1$. The results of $b_{\tilde{n}_e, \tilde{n}_e, \tilde{n}_e}^2(f_1, 4\text{kHz} - f_1)$ as a function of f_1 are plotted in figures 3(c) and (f). The $b_{\tilde{n}_e, \tilde{n}_e, \tilde{n}_e}^2(f_1, 4\text{kHz} - f_1)$, much bigger than noise level in the frequency range $f_1 \sim 50 - 130$ kHz (see figure 3(c)), are more obvious than that in figure 3(b) for $k_1 = 10$ cm⁻¹ microturbulence. This shows strong nonlinear coupling between the fundamental MHD mode with $f_3 \approx 4$ kHz and k_1 microturbulence with frequency pairs $f_1 \sim 50 - 130$ kHz and 4 kHz $- f_1$. Similar coupling can also be seen in figure 3(f), and the fundamental MHD mode is seen to couple with higher frequencies, i.e. $f_1 \sim 100 - 300$ kHz. Although both $k_1 = 10$ cm⁻¹ and $k_4 = 26$ cm⁻¹ microturbulence have been identified to couple with the MHD mode, the coupling frequency range for $k_1 = 10$ cm⁻¹ is narrower than that for $k_4 = 26$ cm⁻¹ microturbulence. This is consistent with the results that higher both mean frequency \bar{f} and spectral width δf for k_4 ($\bar{f} \approx 95$ kHz, $\delta f \approx 100$ kHz) than k_1 ($\bar{f} \approx 73$ kHz, $\delta f \approx 75$ kHz) microturbulence at the time $t = 8.63-8.73$ s. This is also consistent with the theory that microturbulence of higher wavenumber usually has higher corresponding real frequency and broader frequency spectral width. Note that the mean frequency \bar{f} is defined for a wavenumber k with the

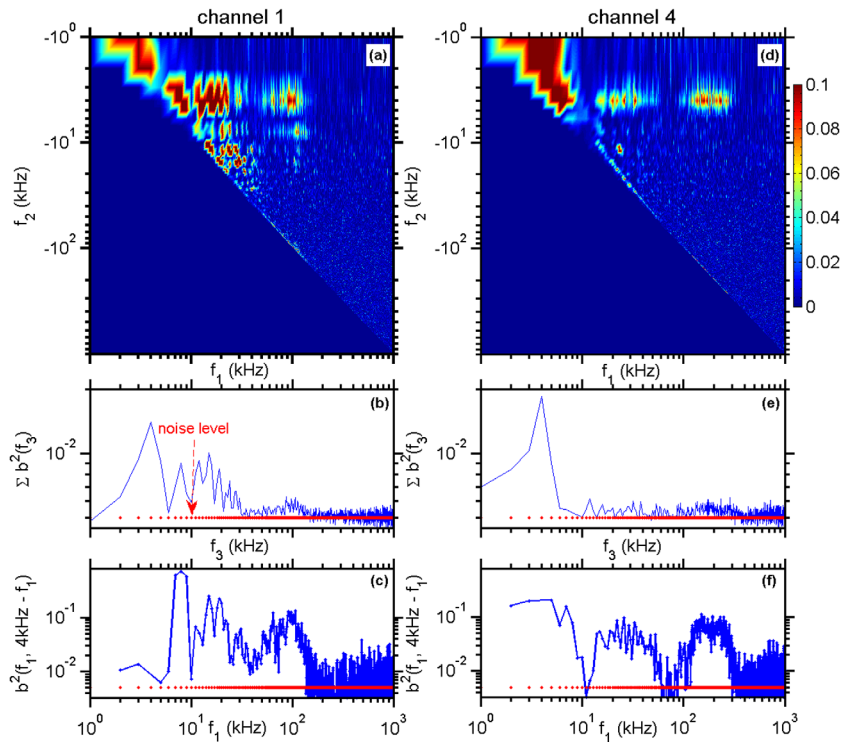


Figure 3. (a) and (d): squared auto-bicoherence $b_{\bar{n}_e, \bar{n}_e, \bar{n}_e}^2(f_1, f_2)$ of density fluctuations from channel 1 ($k_1 = 10 \text{ cm}^{-1}$) and channel 4 ($k_4 = 26 \text{ cm}^{-1}$) respectively; note that panel (a) and (d) share the same colorbar. (b) and (e): summed squared auto-bicoherence $\Sigma b_{\bar{n}_e, \bar{n}_e, \bar{n}_e}^2(f_3)$ (for all f_1 and f_2 satisfying $f_3 = f_1 + f_2$) for channel 1 and channel 4 respectively; (c) and (f) squared auto-bicoherence $b_{\bar{n}_e, \bar{n}_e, \bar{n}_e}^2(f_1, 4 \text{ kHz} - f_1)$ with $f_3 = 4 \text{ kHz}$ (the frequency of fundamental MHD mode) for channel 1 and channel 4 respectively. The bispectral analysis is carried out at $t = 8.63\text{--}8.73 \text{ s}$ with frequency resolution $\Delta f = 1 \text{ kHz}$ and ensemble numbers $N = 200$, note that the red dotted lines denote the noise level $1/N = 0.005$.

expression $\bar{f} = \frac{\Sigma f S_k(f)}{\Sigma S_k(f)}$ and the spectral width δf is from the full width at half maximum of the power spectrum. Finally we note that similar results are also obtained from channel 2 ($k_2 = 18 \text{ cm}^{-1}$) and channel 3 ($k_3 = 10 \text{ cm}^{-1}$) (not shown).

Having established the nonlinear coupling between the MHD mode and microturbulence using bicoherence analysis, we will also explore how the microturbulent amplitude responds to the MHD mode, by employing an envelope modulation method [33]. The envelope of a time series can be calculated using the Hilbert transform. In order to obtain the envelope of the broadband microturbulence signal, first the scattering signals from different channels are high-pass ($f > 50 \text{ kHz}$) filtered, and then the Hilbert transform is applied to the filtered signal set to obtain its envelope. Figure 4(a) plots the power spectrum of the unfiltered scattering signal from channel 1 for $f \in [0, 20] \text{ kHz}$, where multiple harmonics of the MHD mode can be seen. Figure 4(b) plots the power spectrum of the envelope of broadband ($f > 50 \text{ kHz}$) microturbulence, and two spectral peaks can be easily seen at corresponding frequencies of the fundamental and first harmonic of the MHD mode shown in figure 4(a). The coherence between the envelope and the unfiltered channel 1 signal is demonstrated in figure 4(c) where the squared coherence at the frequency of each spectral peak seen in figure 4(b) is much higher than the noise level. These results (see figures 4(a)–(c)) imply that the amplitude of microturbulence is greatly correlated to the fundamental

MHD mode as well as its first harmonic. The cross-correlation between the unfiltered channel 1 signal and the envelope of microturbulence can also provide us the relative phase at the frequency of fundamental MHD mode which is shown for $t = 8.3\text{--}8.95 \text{ s}$ in figure 4(d). It can be seen that the two oscillations, i.e. the fundamental component of the MHD mode and the amplitude oscillation of the microturbulence, is nearly $2n\pi + \pi$ (note that $\Delta\theta$ has a period of $2n\pi$ [43], where n is an integer) out of phase from $t = 8.3\text{--}8.8 \text{ s}$, and there is a fast jump to nearly in phase after $t \approx 8.8 \text{ s}$. The squared coherence is much higher than the noise level throughout the interested time period shown in figure 4(e). Obvious power at the frequency of fundamental MHD mode as well as its first harmonic (see figure 4(f)) can be seen from the spectrogram of the envelope of high-pass ($f > 50 \text{ kHz}$) filtered channel 1 signal. These results imply that the amplitude of microturbulence is correlated to the MHD mode for a long time.

Moreover, envelope analysis results may be affected by the Doppler shift ($f_{\text{Doppler}} = k_t v_t / 2\pi$, where k_t is the toroidal wavenumber of microturbulence and v_t is plasma toroidal flow velocity). The MHD mode can lead to a modulation of the Doppler shift of the microturbulence spectrum, and thus the high-pass ($f > 50 \text{ kHz}$) filtered turbulent density fluctuation may be also modulated even when the microturbulence is not nonlinearly coupled with the MHD mode. In this paper, we note that microturbulent $\vec{k}_1, \vec{k}_2, \vec{k}_4$ have both the same direction and the same location (the same v_t). Therefore, the temporal

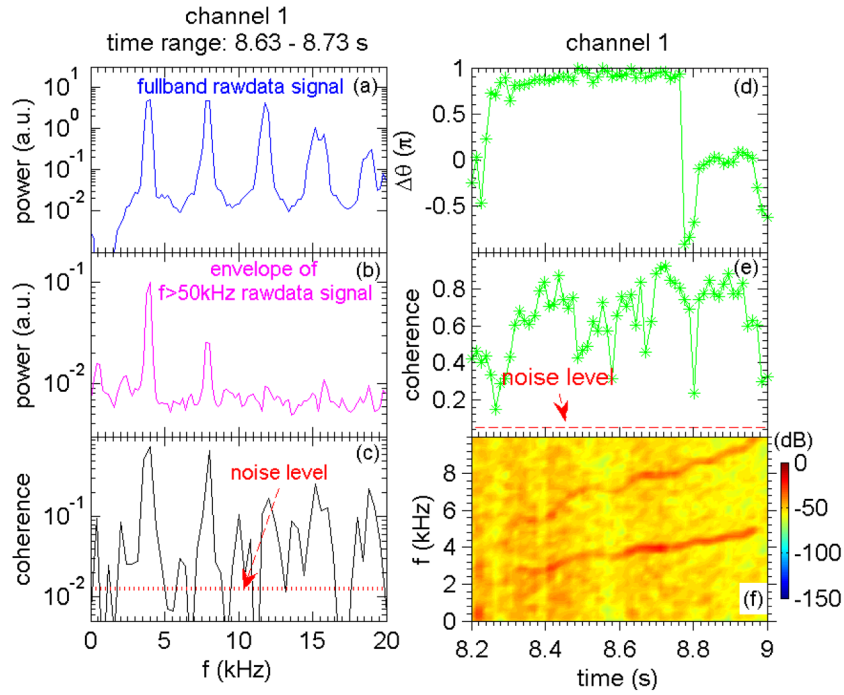


Figure 4. (a) The power spectrum of the scattering signal from channel 1 ($k_1 = 10 \text{ cm}^{-1}$) at $t = 8.63\text{--}8.73 \text{ s}$; (b) the power spectrum of the envelope of high-pass ($f > 50 \text{ kHz}$) filtered signal; (c) the squared coherence between the unfiltered scattering signal and the envelope. (d) The relative phase $\Delta\theta$ between the fundamental frequency component of the MHD mode and the envelope, note that $\Delta\theta \in [2n\pi - \pi, 2n\pi + \pi]$, where n is an integer; (e) squared coherence between the fundamental frequency component of the MHD mode and the envelope; the analysis for (d) and (e) is carried out at $t = 8.2\text{--}9 \text{ s}$ with of frequency resolution $\Delta f = 0.2 \text{ kHz}$, $N = 20$ ensembles and $1/N = 0.05$ for noise level. (f) Spectrogram of the envelope of high-pass ($f > 50 \text{ kHz}$) filtered channel 1 signal.

evolution of $\Delta\theta$ should be the same for $\vec{k}_1, \vec{k}_2, \vec{k}_4$ microturbulence if these microturbulence spectra are modulated only by the Doppler shift effect (not due to microturbulence-MHD interaction). However, our results show that the temporal evolution of the $\Delta\theta$ for k_1 (see figure 4(d)), k_2 and k_4 (not shown for k_2 and k_4) are different. This supports the validity of our envelope analysis results in this paper, and also suggests the existence of microturbulence-MHD multi-scale interaction beyond the Doppler shift effect. The temporal evolution of $\Delta\theta$ is new, and may be related to the nonlinear process. The exact nonlinear coupling mechanism is yet to be determined, and this will be carried out in the future. More importantly, both $k_2 = 18 \text{ cm}^{-1}$ microturbulence (the angle between SP and EP is 0°), and a similar MHD mode have been measured simultaneously (not shown) for another shot 41 167 by our scattering diagnostics. The result from ray tracing calculation shows that wavevector \vec{k}_2 only contains radial wavenumber k_r . Therefore, Doppler shift ($f_{\text{Doppler}} = k_1 v_t / 2\pi$) of k_2 microturbulence should be 0. We observe obvious power of envelope of ($f > 50 \text{ kHz}$) turbulent density fluctuation at frequencies of the fundamental MHD mode as well as its three harmonics (not shown). Meanwhile, we also observe obvious bicoherence between the fundamental MHD mode ($f \approx 2.4 \text{ kHz}$) and $f \in [40, 90] \text{ kHz}$ k_2 microturbulence. These envelope modulation and bicoherence results are obtained in the absence of Doppler shift effect. Therefore, the Doppler shift influence over bispectral or envelope analysis results is limited. This can further support the validity of our bispectral and envelope analysis results on qualitatively identifying microturbulence-MHD mode nonlinear coupling in this paper.

Having identified the nonlinear coupling between (intermediate, small)-scale microturbulence and the MHD mode, here we would like to quantify the temporal evolution of the MHD mode and microturbulence. We integrate the power spectrum over two different frequency bands: $0 < f < 50 \text{ kHz}$ for the MHD mode and $f > 50 \text{ kHz}$ for the microturbulence. The time traces of time-averaged (averaged over a time period much longer than the fundamental cycle of the MHD mode) density fluctuation frequency-integrated spectral power, S_{tot} , for the microturbulence and for the MHD mode are shown in figures 5(b) and (c) respectively, for channel 1 measuring $k_1 = 10 \text{ cm}^{-1}$ microturbulence (equivalent data for channel 4 are shown in figures 5(e) and (f)). We note that both figures 2(e) and 5(a) come from the same data. It can be seen that the lower k ($k_1 = 10 \text{ cm}^{-1}$) (channel 1, figure 5(b)) total spectral power S_{tot} gradually decreases as the coherent mode S_{tot} decreases (see figures 5(c) and (f)), while the higher- k ($k_4 = 26 \text{ cm}^{-1}$) (channel 4, figure 5(e)) total spectral power S_{tot} increase substantially during the same time period as the coherent mode S_{tot} decreases. Some simulation papers [44–46] report that the energy flow can be transferred from microturbulence to MHD modes. However, it is reasonable to expect in this paper that the influence of the MHD mode on microturbulence, through a forward cascade process, may be dominant—i.e. energy is transferred from large scale to small scale due to mode coupling. Moreover, as a drive of microturbulence, the modulation of ∇Te by the MHD mode can directly affect the broadband microturbulence. The multi-scale mechanisms are complex and the MHD mode may affect the lower- k and higher- k components of microturbulence differently. Another

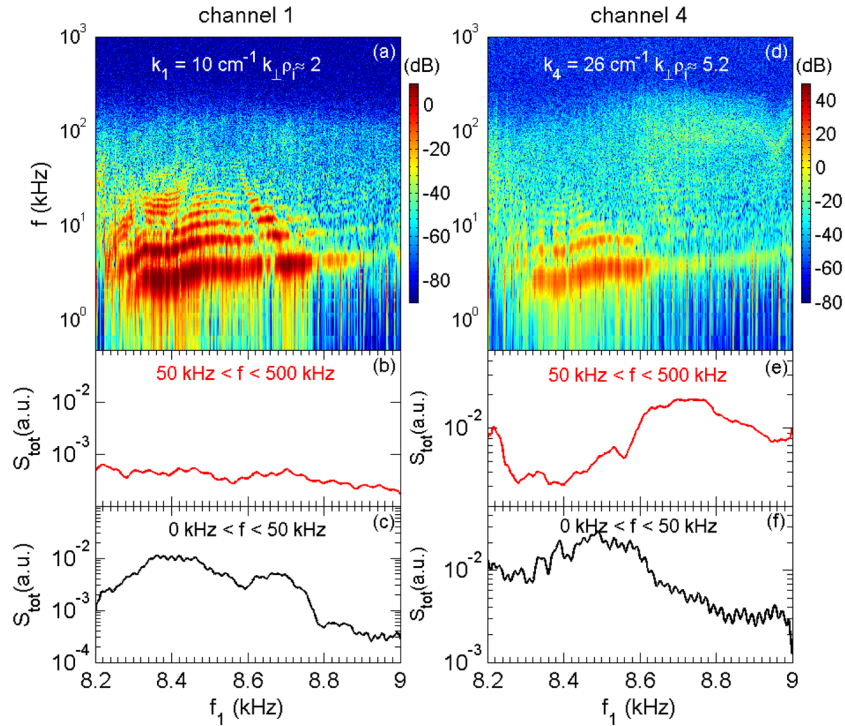


Figure 5. Spectrograms of signals from (a) channel 1 (both the MHD mode and $k_{\perp} = 10 \text{ cm}^{-1}$ microturbulence), (d) channel 4 (both the MHD mode and $k_{\perp} = 26 \text{ cm}^{-1}$ microturbulence). Frequency-integrated spectral power S_{tot} for the microturbulence for $50 < f < 500 \text{ kHz}$: (b) channel 1, (e) channel 4. Frequency-integrated spectral power S_{tot} for the MHD mode for $0 < f < 50 \text{ kHz}$: (c) channel 1, (f) channel 4.

possible reason to explain this is that the modulation of ∇T_e by the MHD mode can change the E_r , and this can further affect the shearing rate $\omega_{\vec{E} \times \vec{B}}$, which has been thought to restrain low- k microturbulence more obviously than high- k , due to its smaller spatial scales and larger linear growth rates [13].

As has been mentioned before, the fundamental MHD mode is identified as $m/n = 1/1$ mode and all the poloidal β_p satisfy $\beta_p > 0.3$ in the presence of this MHD mode. These are consistent with the theoretical critical threshold $\beta_{p,\text{crit}}$ for pressure driven internal kink mode [47]. This MHD mode exists for more than 0.6 s, so we exclude the possibility that this mode is driven by energetic particles, because its confinement is estimated to be less than 0.1 s in EAST (private communication with Dr Wei Chen). Coppi's paper [48] suggests resistive internal kink modes can reconnect and produce configurations with magnetic islands. The MHD mode in this paper saturates quickly, and lasts for a long time (more than 0.6 s) in the nonlinear state, so we guess this mode contains a magnetic island. A phase jump of nearly π occurs between two adjacent soft x-ray channels (not shown, core region), and electron cyclotron emission signals (not shown, core region) also roughly show nearly π phase difference among different channels. These results support the existence of a magnetic island [49], but we cannot know the exact position of the magnetic island, due to the chord averaged signals from soft x-rays, and the uncertainty of detection position from ECE signals in the current ramp-down phase. Nonetheless, this MHD mode has not been fully identified as internal kink mode in experiment, and this mode may have a kink-tearing structure [50]. However, there is no doubt that this MHD mode is located in core plasmas, and both its temporal and spatial scales have a vast separation from the (intermediate,

small)-scale microturbulence. Due to the lack of the measurement of toroidal rotation velocity V_t , we cannot quantitatively estimate the contribution of the possible Doppler shift effect on our bispectral and envelope modulation results in this paper. We will give a detailed study of this in a future paper.

4. Summary

In summary, we have qualitatively identified the nonlinear coupling between the MHD mode ($m = -1$, $n = 1$, $f \approx 4 \text{ kHz}$) and (intermediate, small)-scale microturbulence ($k_{\perp} = 10, 18$ and 26 cm^{-1} , $k_{\perp} \rho_i \sim 2-5.2$) through bicoherence analysis and envelope modulation methodology. Statistically significant bicoherence has been observed between the MHD mode and broadband microturbulence in the bispectral analysis. Clear modulation of the amplitude of $f > 50 \text{ kHz}$ turbulent density fluctuation has been observed at frequencies of the fundamental MHD mode as well as its first harmonic in the envelope modulation analysis. Different temporal evolution of $\Delta\theta$ for k_1, k_2, k_4 microturbulence suggests the existence of microturbulence-MHD multi-scale interaction beyond the Doppler shift effect. Similar results for #41167 (no Doppler shift effect) further supports the validity of our bispectral and envelope analysis results in qualitatively identifying microturbulence-MHD nonlinear coupling in this paper. It is reasonable to expect that the MHD mode can affect microturbulence nonlinearly through forward cascade process, i.e. energy transferring from large scale to small scale due to mode coupling. Quantitative estimation of the possible contribution of the Doppler shift effect on the bispectral and envelope modulation results will be carried out in the future.

Acknowledgments

The author thanks Prof. C.X. Yu, V. Igochine, D.L. Brower, W.X. Ding, W. Chen, Z.X. Wang and Z.R. Wang for their useful discussions. This work has been supported by National Natural Science Foundation of China with Contract Nos. 11505228, 10975159, 11275232, 11575238, 11575235, 11422546, National Key Development Project with Contract No. 2016YFA0400600, National Magnetic Confinement Fusion Science Program of China with Contract No. 2015GB101000 and the Science Foundation of ASIPP with Contact No. Y45ETY2307.

ORCID iDs

B. Lyu  <https://orcid.org/0000-0002-3916-6230>

References

- [1] Coppi B. and Pegoraro F. 1977 *Nucl. Fusion* **17** 969
- [2] Kadomtsev B.B. and Pogutse O.P. 1971 *Nucl. Fusion* **11** 67
- [3] Dorland W. et al 2000 *Phys. Rev. Lett.* **85** 5579
- [4] Ren Y. et al 2017 *Nucl. Fusion* **57** 072002
- [5] Hazeltine R.D. and Strauss H.R. 1976 *Phys. Rev. Lett.* **37** 102
- [6] Drake J.F. et al 1980 *Phys. Rev. Lett.* **44** 994
- [7] Guttenfelder W. et al 2012 *Phys. Plasmas* **19** 022506
- [8] Bardóczi L. et al 2017 *Phys. Plasmas* **24** 062503
- [9] Pouquet A. et al 1976 *J. Fluid Mech.* **77** 321
- [10] Tham P. and Sen A.K. 1994 *Phys. Rev. Lett.* **72** 1020
- [11] Itoh K. et al 2003 *J. Plasma Fusion Res.* **79** 6
- [12] Menard J.E. et al 2011 *Nucl. Fusion* **51** 103014
- [13] Doyle E.J. et al 2007 Progress in the ITER physics basis chapter 2: plasma confinement and transport *Nucl. Fusion* **47** S18
- [14] Horton W. 1999 *Rev. Mod. Phys.* **71** 735
- [15] Diamond P.H. et al 2005 *Plasma Phys. Control. Fusion* **47** R35
- [16] Bierwage A. et al 2005 *Phys. Rev. Lett.* **94** 065001
- [17] Ren Y. et al 2011 *Phys. Rev. Lett.* **106** 165005
- [18] Mazzucato E. et al 2008 *Phys. Rev. Lett.* **101** 075001
- [19] Huysmans G.T.A. et al 2001 *Phys. Rev. Lett.* **87** 245002
- [20] Ren Y. et al 2012 *Phys. Plasmas* **19** 056125
- [21] Ishii Y. et al 2000 *Phys. Plasmas* **7** 4477
- [22] Ren Y. et al 2013 *Nucl. Fusion* **53** 083007
- [23] Rhodes T.L. et al 2007 *Phys. Plasmas* **14** 056117
- [24] Ishizawa A. and Nakajima N. 2007 *Nucl. Fusion* **47** 1540
- [25] Li J.Q. et al 2009 *Nucl. Fusion* **49** 095007
- [26] Hornsby W.A. et al 2010 *Phys. Plasmas* **17** 092301
- [27] Tsui H.Y.W. et al 1993 *Phys. Rev. Lett.* **70** 2565
- [28] Yu C.X. et al 1992 *Nucl. Fusion* **32** 9
- [29] Bardóczi L. et al 2016 *Phys. Rev. Lett.* **116** 215001
- [30] Bardóczi L. et al 2017 *Phys. Plasmas* **24** 056106
- [31] Fernández-Marina F. et al 2017 *Phys. Plasmas* **24** 072513
- [32] Kim Y.C. and Powers E.J. 1979 *IEEE Trans. Plasma Sci.* **PS-7** 120
- [33] Nagashima Y. et al 2005 *Phys. Rev. Lett.* **95** 095002
- [34] Li Y.D. et al 2004 *Plasma Sci. Technol.* **6** 2526
- [35] Li Y.D. et al 2009 *Plasma Sci. Technol.* **11** 5
- [36] Mazzucato E. 2003 *Phys. Plasmas* **10** 753
- [37] Mazzucato E. 2006 *Plasma Phys. Control. Fusion* **48** 1749
- [38] Lao L.L. et al 1985 *Nucl. Fusion* **25** 1611
- [39] Andel H.W.H.V. et al 1987 *Plasma Phys. Control. Fusion* **29** 49
- [40] Deng C.B. and Brower D.L. 2010 *Rev. Sci. Instrum.* **81** 10D503
- [41] Cheng J. et al 2014 *Nucl. Fusion* **54** 114004
- [42] Cheng J. et al 2013 *Phys. Rev. Lett.* **110** 265002
- [43] Hu J.S. et al 2015 *Phys. Rev. Lett.* **114** 055001
- [44] Ishizawa A. and Nakajima N. 2010 *Phys. Plasmas* **17** 072308
- [45] Muraglia M. et al 2011 *Phys. Rev. Lett.* **107** 095003
- [46] Agullo O. et al 2014 *Phys. Plasmas* **21** 092303
- [47] Bussac M.N. et al 1975 *Phys. Rev. Lett.* **35** 1638
- [48] Coppi B. et al 1976 *Fiz. Plazmy* **2** 961
- [49] Chapman I.T. et al 2010 *Nucl. Fusion* **50** 045007
- [50] Tobias B. et al 2013 *Plasma Phys. Control. Fusion* **55** 095006